Broadband high-index prism for asymmetric acoustic transmission

Cite as: Appl. Phys. Lett. **114**, 121902 (2019); https://doi.org/10.1063/1.5092125 Submitted: 07 February 2019 . Accepted: 14 March 2019 . Published Online: 29 March 2019

Ailing Song , Junfei Li , Chen Shen , Xiuyuan Peng , Xiaohui Zhu , Tianning Chen , and Steven A. Cummer







ARTICLES YOU MAY BE INTERESTED IN

Broadband ultrasonic focusing in water with an ultra-compact metasurface lens Applied Physics Letters 114, 104101 (2019); https://doi.org/10.1063/1.5090956

Acoustic perfect absorbers via spiral metasurfaces with embedded apertures Applied Physics Letters 113, 233501 (2018); https://doi.org/10.1063/1.5063289

Acoustic accelerating beam based on a curved metasurface
Applied Physics Letters 114, 113507 (2019); https://doi.org/10.1063/1.5087544





Broadband high-index prism for asymmetric acoustic transmission

Cite as: Appl. Phys. Lett. **114**, 121902 (2019); doi: 10.1063/1.5092125 Submitted: 7 February 2019 · Accepted: 14 March 2019 · Published Online: 29 March 2019







Ailing Song,^{1,2,a)} (D) Junfei Li,² (D) Chen Shen,² (D) Xiuyuan Peng,² (D) Xiaohui Zhu,² (D) Tianning Chen,¹ (D) and Steven A. Cummer^{2,b)} (D)

AFFILIATIONS

School of Mechanical Engineering and State Key Laboratory for Strength and Vibration of Mechanical Structures, Xi'an Jiaotong University, Xi'an, Shaanxi 710049, China

ABSTRACT

Narrow bandwidth and wavefront distortion are two shortcomings of some existing asymmetric acoustic transmission devices. In this letter, we propose a high-index prism for realizing broadband asymmetric acoustic transmission with uniform plane wave outputs. Numerical simulations and experiments are carried out to verify the theoretical prediction. The experimentally measured acoustic pressure fields, the energy transmission contrast, and the refracted angle in the high transmission direction are in good agreement with the numerically simulated results. Both the simulated and measured energy transmission contrast exceeds 10 dB within the broad frequency range of 2000 to 3500 Hz. The broadband performance is attributed to the spiral unit cell employed to construct the prism, which features a high refractive index within a broad bandwidth. Besides, the transmitted waves in the high transmission direction are uniform plane waves. Our approach provides a practical method to design a broadband asymmetric acoustic transmission device with uniform plane wave outputs and has potential in various applications, such as noise control and medical ultrasound.

Published under license by AIP Publishing. https://doi.org/10.1063/1.5092125

Asymmetric acoustic transmission (AAT) devices are devices in which the incident waves from one direction are allowed to transmit through, while those from another direction are blocked. AAT devices can be realized by nonlinear or linear systems and have attracted growing interest due to their potential applications in many fields, such as noise control^{1–3} and medical ultrasound.^{4,5} Liang *et al.*^{6–8} first theoretically and experimentally demonstrated an acoustic diode composed of a nonlinear medium and a superlattice to break time reversal symmetry. To overcome the barriers existing in nonlinear systems (such as frequency conversion, low transmission, narrow bandwidth, and structure complexity),⁹ many researchers devoted to designing linear AAT devices composed of artificial structures, such as phononic crystals, ^{10,11} grating structures, ¹² and acoustic metasurfaces. ^{13,14}

Acoustic metamaterials with an unusual refractive index, including a negative index, ^{15,16} a near-zero index, ^{17,18} and a high index, ¹⁹ offer great potential for the design of AAT devices and have attracted growing attention. Many fascinating phenomena have been realized based on such kinds of acoustic metamaterials, such as negative refraction, ²⁰ acoustic focusing, ^{21,22} and asymmetric acoustic

transmission. ^{23–25} Li *et al.*, ²³ Shen *et al.*, ²⁴ and Jiang *et al.* ²⁵ employed near-zero index materials for realizing the AAT effect. However, these AAT devices still suffer from a limited bandwidth. Many researchers used phononic crystals, ²⁶ gradient-index structures, ²⁷ and acoustic metasurfaces ¹³ to realize the broadband AAT effect, but significant wavefront distortion occurs in these broadband AAT devices. ^{13,26–28} Therefore, it is necessary to explore new methods to solve these problems. In airborne acoustics, some previous studies suggest that the coiling-up space structures, ^{29,30} helical structures, ³¹ and air-filled intercrossing pipes ^{32,33} can be designed to yield a high refractive index with low loss within a relatively broad bandwidth. The high-index structures may be used to design AAT devices with a broad bandwidth and uniform plane wave outputs.

In this letter, we propose a high-index prism composed of spiral unit cells to realize the AAT effect with a broad bandwidth and uniform plane wave outputs at the same time. Theoretical analysis, numerical simulations, and experiments are carried out to verify the behavior of the proposed design. The working principle is that normal refraction or total internal reflection occurs at the interface for

²Department of Electrical and Computer Engineering, Duke University, Durham, North Carolina 27708, USA

a)ailingsong@outlook.com

b)cummer@ee.duke.edu

different incident wave directions. Compared to the previous AAT devices utilizing based on total reflection, ^{23–25} our proposed prism shows a much wider bandwidth. Additionally, the transmitted waves in the positive direction are still uniform plane waves, which is a distinctive advantage over many previous broadband AAT devices. Our design concept provides a practical method to design broadband AAT devices with uniform plane wave outputs.

The proposed acoustic prism is a triangle structure immersed in air, and the prism angle is β , as shown in Fig. 1. The air density is $\rho_{air} = 1.21 \, \text{kg/m}^3$, the sound speed in air is $c_{air} = 343 \, \text{m/s}$, and the refractive index of air is $n_{air} = 1$. The refractive index of the prism n_E is higher than that of air $(n_E > 1)$, which means that the acoustic waves travel slower in the prism than in air. In simulation, the upper and bottom boundaries are perfectly matched layers (PMLs) that can totally absorb the incoming waves. Considering the acoustic waves impinging on the interface between the prism and air, the transmitted waves will travel and obey classical Snell's law

$$\sin(\theta_i) \cdot n_i = \sin(\theta_t) \cdot n_t, \tag{1}$$

where θ_i is the incident angle, θ_t is the refracted angle, n_i is the refractive index of the incident medium, and n_t is the refractive index of the transmitted medium. When acoustic waves travel from the prism into air and the incident angle is greater than the critical angle, total reflection will occur and the critical angle of total reflection is $\theta_c = \sin^{-1}(n_{air}/n_E)$.

When the acoustic waves of left incidence (LI) and right incidence (RI) horizontally impinge on the prism, the wave paths are shown in Figs. 1(a) and 1(b), respectively. The wave paths suggest that the proposed prism can realize the AAT effect by properly designing the prism angle and the refractive index. In the LI case, the acoustic waves refract at interfaces OA and OB and transmit through the prism. The incident angle and the refracted angle at the interface OA are $\theta_{i1} = \beta$ and $\theta_{t1} = \sin^{-1}(\sin \beta \cdot n_{air}/n_E)$, respectively. The incident angle and the refracted angle at the interface OB are $\theta_{i2} = \beta - \theta_{t1}$ and $\theta_{t2} = \sin^{-1}(\sin(\theta_{i2}) \cdot n_E/n_{air})$, respectively. For the acoustic waves to transmit through the interface OB, the incident angle should satisfy $\theta_{i2} < \theta_c$. In the RI case, the normal incident acoustic waves first pass the interface OB. The incident angle at the interface OA ($\theta_{i3} = \beta$) should satisfy the total reflection condition $\theta_{i3} > \theta_c$. In this paper, n_E is set to 2.0 at 3000 Hz. Therefore, the prism angle should satisfy $30^{\circ} < \beta < 54^{\circ}$ to realize the AAT effect. Here, β is chosen as 41°.

We adopt the spiral unit cell to achieve the required refractive index and broadband high transmission. Figure 2(a) shows the

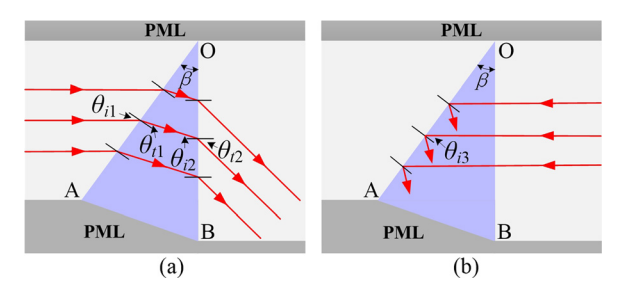


FIG. 1. Schematic view of the high-index prism. The red arrow lines indicate the wave paths in (a) LI and (b) RI cases.

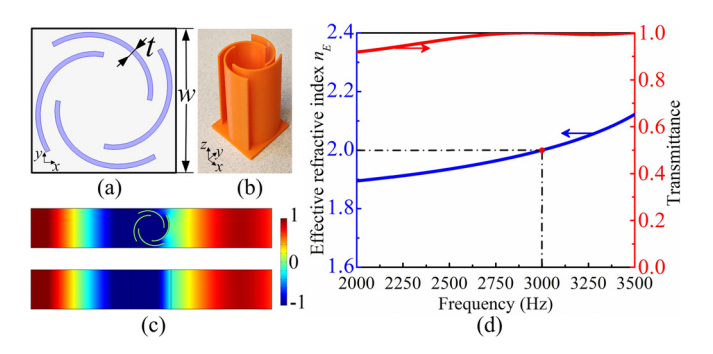


FIG. 2. (a) Cross-sectional view of the unit cell. (b) Photograph of the 3D printed unit cell. (c) Simulated acoustic pressure fields for the unit cell (upper panel) and the effective medium (lower panel). (d) Refractive index and transmittance of the unit cell as a function of frequency.

schematic view of the unit cell composed of four identical spiral walls with rotational symmetry, and this unit cell has a good isotropic property. The geometrical shape of the spiral walls can be described by the Archimedean spiral

$$r(\alpha) = ae^{b\alpha}(\alpha_1 < \alpha < \alpha_2), \tag{2}$$

where $r(\alpha)$ is the radial distance, a and b are coefficients, and α is the spiral angle. The required effective refractive index can be obtained by tuning the parameters of the Archimedean spiral. A retrieval method is used to calculate the effective refractive index from the reflection and transmission coefficients of the unit cell.³⁶ When n_E is 2.0, the parameters of the spiral wall are $t = 0.6 \,\mathrm{mm}$, $w = 18 \,\mathrm{mm}$, $a = 6 \,\mathrm{mm}$, b = 0.21, and $\alpha_1 = 0$, $\alpha_2 = 130^\circ$. Figure 2(b) shows the photograph of a 3D printed unit cell fabricated with acrylonitrile butadiene styrene (ABS) thermal plastic via 3D printing technology. To verify the correctness of the calculated refractive index, we simulate the pressure fields for the unit cell and the effective medium using COMSOL Multiphysics, as shown in Fig. 2(c). For the effective medium, the density is 3.8 kg/m³ and the sound speed is 171.5 m/s. We can see that these two pressure field distributions agree well with each other, which demonstrates the validity of the effective medium model. The refractive index and transmittance at different frequencies are calculated and shown in Fig. 2(d). Within the frequency range of 2000-3500 Hz, the refractive index gradually increases from 1.89 to 2.12, and the transmittance is higher than 90% within the frequency range.

By periodically arranging the spiral unit cells in a square lattice, we can obtain the high-index prism. Numerical simulations are first carried out to validate the performance of the proposed prism. A Gaussian beam of 3000 Hz is incident from the left and right side of the prism, respectively. We first demonstrate the acoustic performance in the ideal effective medium, as shown in Fig. 3(a). It is clearly seen that the AAT effect is realized by the effective medium, which verifies our design strategy. Then, we simulate the acoustic pressure fields in the proposed high-index prism with a real structure, as shown in Fig. 3(b). In the LI case, the acoustic waves can pass the acoustic prism with high transmission. The transmitted waves are still uniform plane waves. In the RI case, the incident waves first normally transmit through the vertical interface and then undergo total reflection at the other interface. Therefore, the acoustic waves cannot pass the prism and the transmitted pressure is nearly zero.

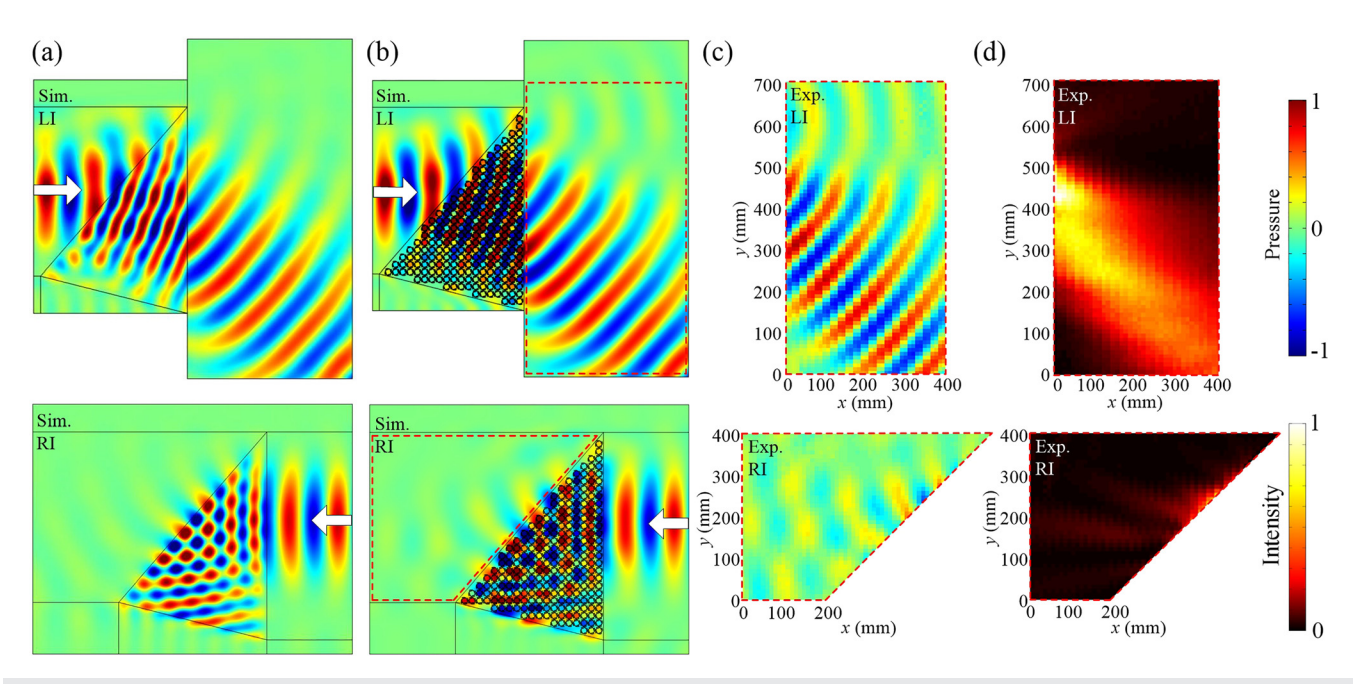


FIG. 3. Acoustic field patterns in the LI case (upper panels) and the RI case (lower panels) excited by a Gaussian beam of 3000 Hz. (a) Simulated acoustic pressure fields in the effective medium. (b) Simulated acoustic pressure fields in the high-index prism composed of spiral unit cells. (c) Measured acoustic pressure fields. (d) Measured acoustic intensity fields.

Then, the experiments are performed in a 2D waveguide to verify the simulation results. The 3D printed sample is shown in Fig. 4(a), and the prism size is labeled. The experimental setup is shown in Fig. 4(b), where the sample is placed between two parallel glass plates. The height of the sample is 40 mm, the same as the distance between two glass plates. The cutoff frequency of the 2D waveguide is 4287 Hz, which is above the working frequency of the prism to ensure 2D wave propagation. Wedge-shaped sound-absorbing foams are placed at the open boundaries of the waveguide to mimic an anechoic environment. A speaker array with 28 speakers is used to generate a Gaussian beam. The field in the scan area is mapped by a moving microphone with the step of 1 cm. A Gaussian modulated sinusoidal pulse with a center frequency of 3000 Hz is sent out by the speakers, and signals at different positions are recorded by the microphone. The collected time-domain signals are time windowed to eliminate boundary reflections and then Fourier transformed to obtain the acoustic fields at different frequencies.3

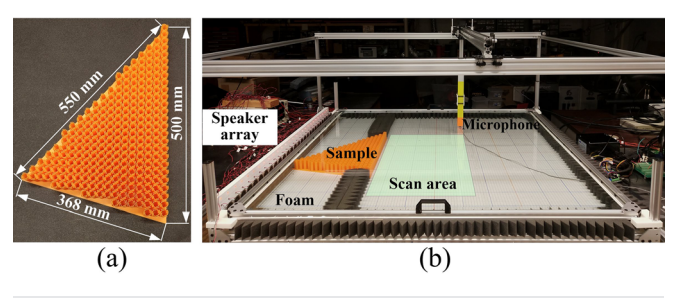
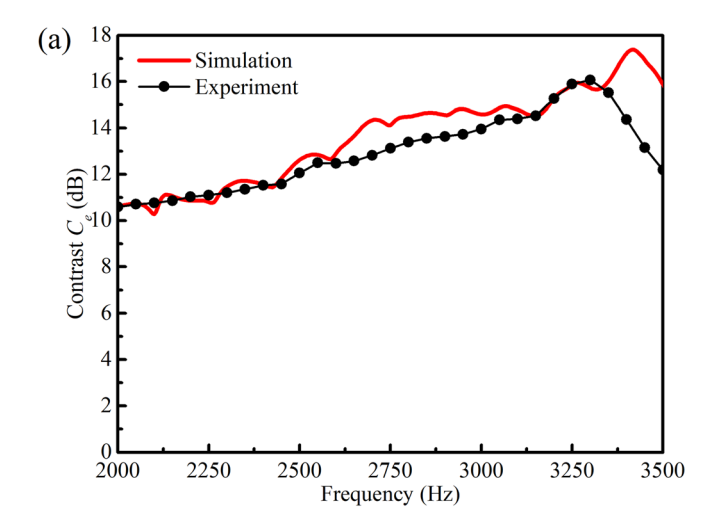


FIG. 4. (a) Photograph of the 3D printed sample. (b) Experimental setup.

The areas marked by the red dotted boxes in Fig. 3(b) are scanned by the moving microphone. The measured real parts of the acoustic pressure fields are shown in Fig. 3(c), showing good agreement with the simulated ones. The transmitted waves in the LI case are still uniform plane waves. In the RI case, the wavelength along the interface OA ($\lambda_{OA} = 8.5$ cm) is smaller than that in air ($\lambda_{air} = 11.4$ cm), and so, the wave number along the interface OA $(k_{\parallel}=2\pi/\lambda_{OA})$ is larger than that in air $(k_{air}=2\pi/\lambda_{air})$. Due to the relation, $k_{\parallel}^2+k_{\perp}^2$ $=k_{air}^2$, the wave number perpendicular to the interface OA (k_{\perp}) becomes imaginary. Therefore, the transmitted waves at the interface OA become evanescent, which decay rapidly along the normal direction and do not contribute to the far fields.³⁸ The measured acoustic intensity fields are shown in Fig. 3(d). We can observe strong acoustic intensity distributions in the LI case and weak acoustic intensity distributions in the RI case. Both the simulated and measured results demonstrate the AAT performance of the proposed prism.

Although the proposed prism is effective at 3000 Hz, it is necessary to analyze the bandwidth. As shown in Fig. 2(d), the refractive index and the transmission coefficient remain high within a broad bandwidth, which suggests the possibility of the AAT effect in a broad bandwidth. We calculate and compare the energy transmission contrast in both simulations and experiments, as shown in Fig. 5(a). Due to the fact that the test frequency of the 2D waveguide is limited by its size, we only present the simulation and measured results from 2000 Hz to 3500 Hz. The energy transmission contrast C_e is defined as the ratio between the total transmitted energy in the LI and RI cases. The total transmitted energy is obtained by integrating the acoustic energy along a line 10 cm away from the sample. The simulated and measured energy transmission contrast at 3000 Hz is 14.5 dB and 14.1 dB, respectively. The measured energy transmission contrast



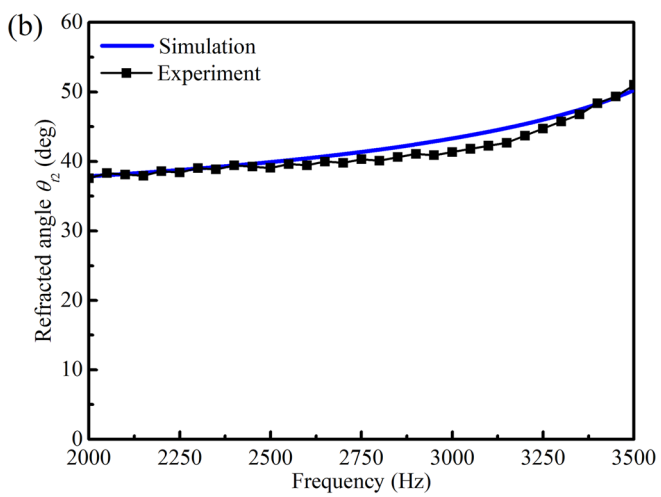


FIG. 5. (a) Energy transmission contrast in simulations (red line) and experiments (black dots). (b) Refracted angle in simulations (blue line) and experiments (black squares) in the LI case.

agrees well with the simulated one, despite some small deviations. Both the simulated and measured energy transmission contrast exceeds 10 dB within the frequency range of 2000 to 3500 Hz, indicating the broadband AAT performance of the proposed prism. The broadband performance is attributed to the spiral unit cell employed for designing the prism, which can maintain a high refractive index within the broad bandwidth.

In the LI case, the acoustic waves can pass the prism and the transmitted wave direction can be described by the refracted angle θ_{t2} . It is necessary to compare the simulated and measured refracted angles, as shown in Fig. 5(b). The energy distributions in each direction are calculated by performing Fourier transform along a line right behind the high-index prism; then, the refracted angle can be determined. The variation tendency of the measured refracted angle agrees well with that of the simulated refracted angle. When we increase the frequency from 2000 Hz to 3500 Hz, θ_{t2} gradually increases.

Therefore, the transmitted waves gradually deviate from the normal direction of the interface OB. The small discrepancies between the simulated and measured results in Fig. 5 may be caused by several factors. The inevitable internal loss can result in smaller transmission in experiments than in simulations. The imperfect boundaries of the 2D waveguide may cause some unwanted reflections from the boundaries. Besides, the fabrication errors may result in the existence of small gaps between the top glass plate and the sample's upper surface. The gaps may cause some sound leakage.

In summary, we report on the theoretical analysis, numerical simulations, and experimental demonstration of a high-index prism capable of realizing the broadband AAT effect with uniform plane wave outputs. The prism angle is carefully designed, and the spiral unit cells are used to achieve the required effective refractive index. The experimental results agree well with the theoretical analysis and simulated results. Both the simulated and measured acoustic pressure fields show that the proposed prism can realize the AAT effect, and the transmitted waves in the high transmission direction are still uniform plane waves. The simulated and measured energy transmission contrast exceeds 10 dB within the broad frequency range of 2000 to 3500 Hz. The broadband performance is attributed to the high-index spiral unit cell employed for designing the prism. Our design concept provides a practical way to design broadband AAT devices and has potential in various applications, such as noise control and medical ultrasound

This work was supported by a Multidisciplinary University Research Initiative grant from the Office of Naval Research (N00014-13-1-0631), an Emerging Frontiers in Research and Innovation grant from the National Science Foundation (No. 1641084), and the National Natural Science Foundation of China (No. 51675402). A.L.S. also acknowledges the scholarship from the Chinese Scholarship Council (No. 201806280160).

REFERENCES

¹S. A. Cummer, Science **343**, 495 (2014).

²H. L. Zhang, Y. F. Zhu, B. Liang, J. Yang, J. Yang, and J. C. Cheng, Appl. Phys. Lett. 111, 203502 (2017).

Y. Ge, H. X. Sun, S. Q. Yuan, and Y. Lai, Appl. Phys. Lett. 112, 243502 (2018).
 J. P. Xia, X. T. Zhang, H. X. Sun, S. Q. Yuan, J. Qian, and Y. Ge, Phys. Rev. Appl. 10, 014016 (2018).

D. Monroe, Phys. Rev. Focus 24, 8 (2009), https://physics.aps.org/story/v24/st8.
 B. Liang, B. Yuan, and J. C. Cheng, Phys. Rev. Lett. 103, 104301 (2009).

⁷B. Liang, X. S. Guo, J. Tu, D. Zhang, and J. C. Cheng, Nat. Mater. **9**, 989 (2010).

⁸B. Liang, X. Y. Zou, B. Yuan, and J. C. Cheng, Appl. Phys. Lett. **96**, 233511 (2010).

⁹A. Cicek, O. A. Kaya, and B. Ulug, Appl. Phys. Lett. **100**, 111905 (2012).

¹⁰ A. L. Song, T. N. Chen, X. P. Wang, and L. L. Wan, J. Appl. Phys. **120**, 085106 (2016).

¹¹S. Zhang, Y. Zhang, Y. J. Guo, Y. H. Leng, W. Feng, and W. W. Cao, Phys. Rev. Appl. 5, 034006 (2016).

¹²H. X. Sun, S. Q. Yuan, and S. Y. Zhang, Appl. Phys. Lett. 107, 213505 (2015).

¹³Y. F. Zhu, X. Y. Zou, B. Liang, and J. C. Cheng, Appl. Phys. Lett. **106**, 173508 (2015).

¹⁴Y. Li, C. Shen, Y. B. Xie, J. F. Li, W. Q. Wang, S. A. Cummer, and Y. Jing, Phys. Rev. Lett. 119, 035501 (2017).

¹⁵L. Fok and X. Zhang, Phys. Rev. B 83, 214304 (2011).

¹⁶Y. B. Xie, B. I. Popa, L. Zigoneanu, and S. A. Cummer, Phys. Rev. Lett. 110, 175501 (2013).

¹⁷Q. Wei, Y. Cheng, and X. J. Liu, Appl. Phys. Lett. **102**, 174104 (2013).

- ¹⁸M. Dubois, C. Z. Shi, X. F. Zhu, Y. Wang, and X. Zhang, Nat. Commun. 8, 14871 (2017).
- ¹⁹Z. X. Liang and J. Li, Phys. Rev. Lett. **108**, 114301 (2012).
- ²⁰B. Y. Liu, B. Ren, J. J. Zhao, X. D. Xu, Y. X. Feng, W. Y. Zhao, and Y. Y. Jiang, Appl. Phys. Lett. **111**, 221602 (2017).
- ²¹Y. Li, B. Liang, X. Tao, X. F. Zhu, X. Y. Zou, and J. C. Cheng, Appl. Phys. Lett. 101, 233508 (2012).
- ²²Y. Li, G. K. Yu, B. Liang, X. Y. Zou, G. Y. Li, S. Cheng, and J. C. Cheng, Sci. Rep. 4, 6830 (2014).
- ²³Y. Li, B. Liang, Z. M. Gu, X. Y. Zou, and J. C. Cheng, Appl. Phys. Lett. **103**, 053505 (2013).
- C. Shen, Y. B. Xie, J. F. Li, S. A. Cummer, and Y. Jing, Appl. Phys. Lett. 108, 223502 (2016).
- 25 X. Jiang, B. Liang, X. Y. Zou, J. Yang, L. L. Yin, J. Yang, and J. C. Cheng, Sci. Rep. 6, 28023 (2016).
- ²⁶B. Yuan, B. Liang, J. C. Tao, X. Y. Zou, and J. C. Cheng, Appl. Phys. Lett. 101, 043503 (2012).
- ²⁷R. Q. Li, B. Liang, Y. Li, W. W. Kan, X. Y. Zou, and J. C. Cheng, Appl. Phys. Lett. 101, 263502 (2012).

- ²⁸ A. L. Song, T. N. Chen, X. P. Wang, and Y. H. Xi, Phys. Lett. A 381, 2283 (2017).
- ²⁹Y. Li, B. Liang, X. Y. Zou, and J. C. Cheng, Appl. Phys. Lett. **103**, 063509 (2013).
- 30Y. Y. Fu, J. F. Li, Y. B. Xie, C. Shen, Y. D. Xu, H. Y. Chen, and S. A. Cummer, Phys. Rev. Mater. 2, 105202 (2018).
- ³¹X. F. Zhu, K. Li, P. Zhang, J. Zhu, J. T. Zhang, C. Tian, and S. C. Liu, Nat. Commun. 7, 11731 (2016).
- ³²F. Zangeneh-Nejad and R. Fleury, New J. Phys. **20**, 073001 (2018).
- ³³F. Zangeneh-Nejad and R. Fleury, Sci. Rep. **8**, 10401 (2018).
- ³⁴Y. B. Xie, A. Konneker, B. I. Popa, and S. A. Cummer, Appl. Phys. Lett. 103, 201906 (2013).
- 35Y. B. Xie, W. Q. Wang, H. Y. Chen, A. Konneker, B. I. Popa, and S. A. Cummer, Nat. Commun. 5, 5553 (2014).
- ³⁶V. Fokin, M. Ambati, C. Sun, and X. Zhang, Phys. Rev. B **76**, 144302 (2007).
- ³⁷J. F. Li, C. Shen, A. Díaz-Rubio, S. A. Tretyakov, and S. A. Cummer, Nat. Commun. 9, 1342 (2018).
- ³⁸J. F. Li, W. Q. Wang, Y. B. Xie, B. I. Popa, and S. A. Cummer, Appl. Phys. Lett. 109, 091908 (2016).